



UNIVERSITAT POLITÈCNICA DE CATALUNYA  
BARCELONATECH

Escola Superior d'Enginyeries Industrial,  
Aeroespacial i Audiovisual de Terrassa

UPC ESEIAAT

SPACE PROPULSION: PROJECT 2

---

# Hall Thruster

---

**Authors:**

**Jorge Simón**

**Iñaki Fernandez**

**Deadline:**

January 2024

# Index

<b>1</b>	<b>Background and State of the Art</b>	<b>3</b>
<b>2</b>	<b>Hall Thruster Description</b>	<b>5</b>
<b>3</b>	<b>Numerical Analysis</b>	<b>7</b>
3.1	Question . . . . .	9
3.2	Question . . . . .	12
3.3	Question . . . . .	15
<b>4</b>	<b>Conclusions</b>	<b>18</b>

# 1 Background and State of the Art

Electric propulsion, finds its roots in the early 20th century, pioneered independently by like Robert Goddard [1] and Tsiolkovskiy [2] in 1906 and 1911, respectively. The systematic exploration of electric propulsion systems began with Ernst Stuhlinger's [3] comprehensive analysis in 1964, marking a crucial turning point. The foundational understanding of electric propulsion thrusters emerged in 1968 through Robert Jahn's [4] seminal work, providing detailed insights into the physics of these systems. Over subsequent years, various textbooks elaborated on the basics of electric propulsion, fostering a growing comprehension of its principles.

The 1960s witnessed the establishment of significant electric propulsion research programs globally. Experimental ion thrusters, launched into orbit in the early 1960s, set the stage for continued developments in ion and Hall thrusters. Russia emerged as a pioneer in practical applications, notably employing Hall thrusters for station-keeping on communications satellites since 1971 [5]. Japan and the United States followed suit in 1995 and 1997, respectively, with their own ion thruster systems.

The commercialization of ion thrusters gained momentum in the late 1990s, with notable milestones such as the launch of NASA's Solar Electric Propulsion Technology Applications Readiness (NSTAR) ion thruster in 1998. The past two decades witnessed a steady global growth in the use of electric propulsion in spacecraft, particularly in communications satellites and deep-space scientific missions. Ion and Hall thrusters played a pivotal role in reducing propellant mass for station-keeping applications, with the U.S. and Russia leading the way.

Hall thrusters stand out as intriguing examples of cross-field devices, generating and maintaining large electric fields in the bulk plasma. Their unique characteristics, achieving significantly high current densities, make Hall thrusters a preferred choice for certain applications. The complex interplay of electric and magnetic fields, as observed in  $E \times B$  devices, underscores the importance of avoiding the Hall effect to ensure optimal electron confinement and conductivity. The intricate balance of magnetic and electric fields in Hall thrusters, coupled with their closed-drift geometry, positions them as key players in space propulsion.

The innovative Hall Thrusters, also known as Stationary Plasma Thrusters (SPT), have attracted extensive research efforts globally due to their enhanced efficiency, reduced propellant costs, and versatility in addressing a diverse range of space exploration missions.

The deployment of Hall thrusters in actual space missions began with the European Space Agency's (ESA) lunar mission, SMART-1, in 2003. Subsequently, the Naval Research Laboratory's (NRL) STEX spacecraft featured the first Hall thruster on a Western satellite, utilizing the Russian D-55. The Busek BHT-200 marked the first American Hall thruster in space on the TacSat-2 technology demonstration spacecraft. Another milestone was achieved with the Aerojet BPT-4000, the highest power Hall thruster ever flown in space, launching in August 2010 on the military Advanced Extremely High-Frequency GEO

communications satellite. This thruster, with a power of 4.5 kW, not only performed stationkeeping tasks but also provided orbit-raising capabilities.

The commercial sector has embraced Hall thruster technology, with notable examples including SpaceX's Starlink constellation. The Starlink satellites, constituting the largest satellite constellation globally, utilize Hall-effect thrusters for various purposes. SpaceX's innovative use of argon as a propellant in these thrusters, as opposed to the more expensive krypton, has not only increased thrust but has also contributed to cost savings. Elon Musk, the CEO of SpaceX, highlighted the strategic shift to argon, emphasizing its abundance compared to the rare krypton.

A significant step in the evolution of Hall thruster applications occurred with the Psyche spacecraft, which was launched in 2023. This spacecraft, equipped with Hall thrusters, embarked on a mission to explore 16 Psyche within the Asteroid Belt, representing the first deployment of Hall thrusters beyond Earth's sphere of influence. In parallel, at the forefront of Hall thruster development is the University of Michigan's Plasmadynamics and Electric Propulsion Laboratory (PEPL), which introduced the X3 Nested Channel Hall Thruster. As of 2021, the X3 stands as the highest power Hall-effect thruster in development. With a remarkable power capacity of 100 kW, a diameter of approximately 80 cm, and a weight of 230 kg, the X3 represents a significant leap forward in Hall thruster capabilities.

The nested-channel design of the X3 is identified as a key innovation to increase power levels beyond 100 kW while maintaining acceptable device size and mass. NASA, recognizing the potential of high-power electric propulsion (up to 300 kW), has identified such technologies as enabling for a variety of mission structures, including human space exploration. The X3, a three-channel nested Hall thruster is designed to operate efficiently with both krypton and xenon propellants, featuring a discharge voltage range of 200–800 V and a total discharge current capacity of up to 250 A. Remarkably, the thruster's power throttling range spans from 2 kW to 200 kW, offering unprecedented flexibility in adapting to mission requirements.

The successful development and testing of the X3 highlight the capability of Hall thrusters and NHTs for applications in cargo and crew transport, positioning this technology as a vital component in the roadmap to Mars. The X3, with its advanced features and impressive performance metrics, represents a substantial advancement in the quest for efficient and powerful propulsion systems for ambitious space exploration missions.

Another state of the art Hall Thruster is the NASA HERMeS Hall Thruster, which has been designed for the Gateway of the ARTEMIS program [6]. The HERMeS Hall Thruster is designed to operate at 13 kW, offering a specific impulse of 3000 s and a lifetime exceeding 50000 hours. Its maximum thrust is approximately 600 mN, with an efficiency of 68.2%. For the Gateway purposes, the NASA HERMES Hall Thruster provides a balance of high specific impulse and thrust with a relatively small power source.

## 2 Hall Thruster Description

Hall thrusters, operate based on the interaction between electric and magnetic fields within a plasma channel. There are two main types of Hall thrusters discussed in the literature, each characterized by the nature of the channel wall: those with dielectric walls and those with metallic walls, the former ones known as thrusters with anode layer (TAL).

### Hall Thruster with Dielectric Walls.

In the Hall thruster with dielectric walls, a key feature is the use of a dielectric insulating wall in the plasma channel, typically made of materials like boron nitride (BN) or borosil (BN-SiO<sub>2</sub>). The thruster's design includes an electrically biased metallic anode at the base of an annular channel, where most of the propellant gas is injected. Additional propellant is injected through an exterior hollow cathode. A scheme of this type of Hall thruster have been depicted in Fig. 1, which was taken from Gobels et al. *Fundamentals of Electric Propulsion: Ion and Hall Thrusters, Chapter 7*.

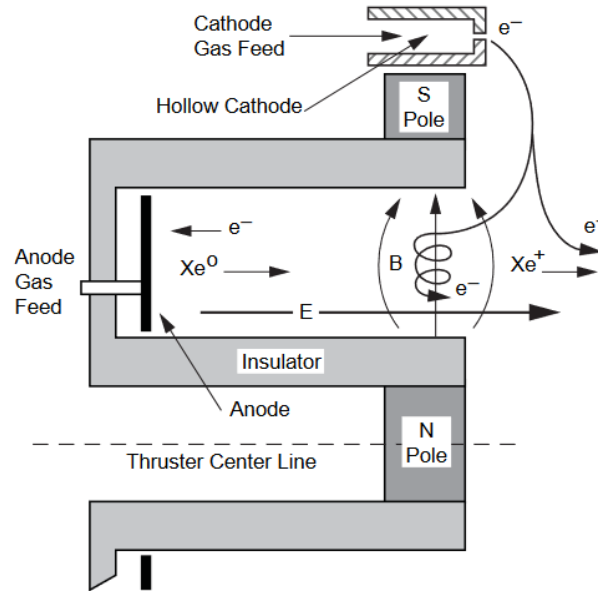


**Figure 1:** Cross-section schematic of a Hall Thruster with dielectric walls. The thruster is composed by an anode, a cathode and a magnetic and electric field. The path of the ions and electrons are also shown [7].

The axial electric field is established between the anode and the hollow-cathode, while a transverse (radial) magnetic field prevents direct electron flow to the anode. Instead, electrons spiral along magnetic field lines and diffuse to the anode and channel walls. This diffusion is typically greater than one can expect, giving rise to the problem of the *anomalous electron transport* [8]. The crossed electric and magnetic fields efficiently ionize the propellant, generating a plasma discharge. Ions from this plasma bombard and erode the dielectric walls, limiting the thruster's lifespan. The reduced axial electron mobility, due to the transverse magnetic field, allows for efficient ionization and by the applied

electric field the ions are accelerated, forming the thrust beam. It is interesting to remark that with the electrons provided by the cathode, the system remains electrically neutral.

### Thruster with Anode Layer (TAL).

The TAL thruster (depicted in Fig. 2) replaces the dielectric channel wall with a metallic conducting wall. This modification shortens the electric field region near the anode, but the fundamental ion generation and acceleration method remain the same. The metallic channel walls are biased negatively to repel electrons, reducing electron-power losses. The TAL thruster's exit plane features metallic guard rings biased at cathode potential to minimize electron loss along field lines.

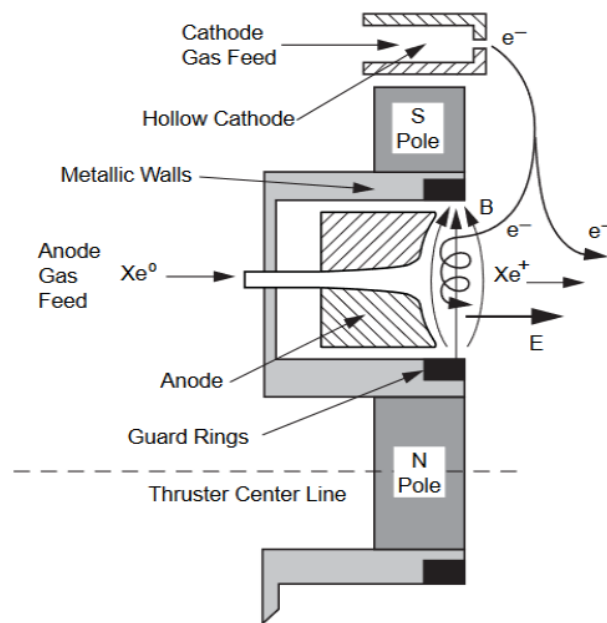


**Figure 2:** *Cross-section schematic of a TAL Hall thruster. The thruster is composed by an anode, a cathode and a magnetic and electric field. The path of the ions and electrons are also shown. In this case, the walls are metallic [7].*

The anode in TAL thrusters extends close to the thruster exit and is shaped to constrain the neutral gas and plasma to the channel center, away from guard rings. The external hollow cathode provides electrons for the discharge and neutralization of the ion beam.

### Operation Principles.

Both types of Hall thrusters utilize the interaction of electric and magnetic fields to ionize propellant and accelerate ions to generate thrust. The azimuthal drift of electrons, influenced by the crossed fields, leads to a "closed-drift" behavior. In Hall thrusters, wall sheath electric fields and the force associated with the magnetic gradient in the radial direction create closed-drift electron motion. The radial magnetic field gradient forms an ion lens, deflecting ions away from channel walls and focusing them into the thrust beam.

The efficiency of Hall thrusters is enhanced by the curvature of magnetic field lines near the exit, particularly for high-voltage, high-specific-impulse designs.

In summary, Hall thrusters are electrostatic devices that leverage electric and magnetic fields to efficiently ionize and accelerate propellant, producing a high-thrust, high-specific-impulse propulsion system for space applications. The choice of dielectric or metallic walls in the thruster design impacts the electric field distribution and the erosion patterns, influencing the overall performance and lifespan of the device.

### 3 Numerical Analysis

In this section, a numerical analysis of a one-dimensional Hall Thruster will be conducted. It will be considered that at the anode, the Mach number is -1, and the exit of the channel is the sonic point, which we can refer to as the Mach number 1 point. Figure 3 illustrates a schematic of the 1D model.

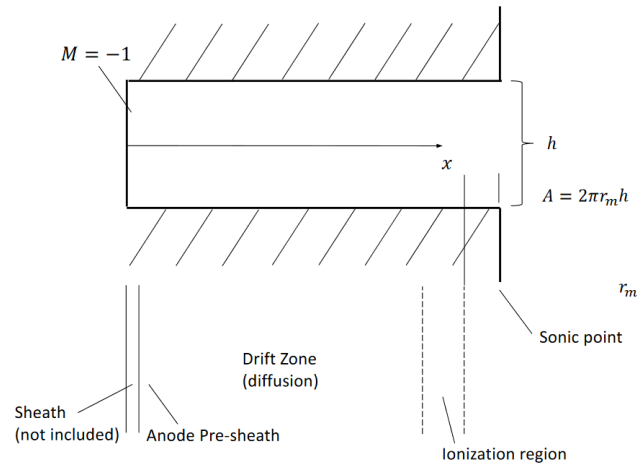


**Figure 3:** *One dimension Hall Thruster model. Figure has been taken from [9].*

As suggested in the project statement, it is recommended to work with non-dimensional variables, using the following as fundamental magnitudes:

$$l_* = 0.01 \text{ m} ; \quad T_* = E_i ; \quad \sigma_* = \sigma_0 \frac{m_i}{m_e} \quad (1)$$

Here,  $E_i$ ,  $\sigma_0$ ,  $m_i$ , and  $m_e$  represent the ionization energy, cross-sectional area, ion mass, and electron mass, respectively. To work with non-dimensional magnitudes, it is necessary to define the normalized velocity, rate of collisions, number density, and particle flux as follows:

$$v_* = \frac{T_*}{m_i} \quad ; \quad \nu_* = \frac{v_*}{l_*} \quad ; \quad n_* = \frac{1}{\sigma_* l_*} \quad ; \quad \Gamma_* = n_* v_* \quad (2)$$

The non-dimensional governing equations of the 1D Hall Thruster can be expressed as follows [9]:

$$\left[ \frac{5}{3} \hat{T}_e - \hat{v}_i^2 \right] \frac{d\hat{v}_i}{d\hat{x}} = \frac{5}{3} \left( \hat{v}_i - \frac{\hat{\Gamma}_d}{\hat{n}_e} \right) \hat{\nu}_e \hat{v}_i + \nu_{ion} \left\{ \frac{5}{3} \hat{T}_e + \hat{v}_i (\hat{v}_i - \hat{v}_n) - \frac{\hat{v}_i}{\hat{v}_{ex}} \left( \frac{2}{3} \hat{E}'_i + \frac{5}{3} \hat{T}_e \right) \right\} \quad (3)$$

$$\left[ \frac{5}{3} \hat{T}_e - \hat{v}_i^2 \right] \frac{d\hat{n}_e}{d\hat{x}} = -\frac{5}{3} \frac{m_e}{m_i} \hat{n}_e \hat{v}_{ex} \hat{\nu}_e - \hat{n}_e \nu_{ion} \left\{ (2\hat{v}_i - \hat{v}_n) - \left[ \frac{2}{3} \hat{E}'_i + \frac{5}{3} \hat{T}_e \right] \frac{1}{\hat{v}_{ex}} \right\} \quad (4)$$

$$\left[ \frac{5}{3} \hat{T}_e - \hat{v}_i^2 \right] \frac{d\hat{T}_e}{d\hat{x}} = -\frac{2}{3} \hat{v}_i^2 \frac{m_e}{m_i} \hat{v}_{ex} \hat{\nu}_e - \nu_{ion} \left\{ \frac{2}{3} \hat{T}_e (2\hat{v}_i - \hat{v}_n) - \left( \frac{\hat{v}_i^2 - \hat{T}_e}{\hat{v}_{ex}} \right) \left( \frac{2}{3} \hat{E}'_i + \frac{5}{3} \hat{T}_e \right) \right\} \quad (5)$$

$$\left[ \frac{5}{3} \hat{T}_e - \hat{v}_i^2 \right] \frac{d\hat{\phi}}{d\hat{x}} = -\frac{5}{3} \frac{m_e}{m_i} \hat{v}_{ex} \hat{\nu}_e \hat{v}_i^2 - \nu_{ion} \left\{ \frac{5}{3} \hat{T}_e (2\hat{v}_i - \hat{v}_n) - \frac{\hat{v}_i^2}{\hat{v}_{ex}} \left[ \frac{2}{3} \hat{E}'_i + \frac{5}{3} \hat{T}_e \right] \right\} \quad (6)$$

where,

$$\hat{v}_{ex} = \left( \hat{v}_i - \frac{\hat{\Gamma}_d}{\hat{n}_e} \right) \quad ; \quad n_n = n_* \left( \frac{\hat{\Gamma}_m}{\hat{c}_n} - \hat{n}_e \frac{\hat{v}_i}{\hat{c}_n} \right) \quad (7)$$

$$\hat{\nu}_{en} = \left( \frac{\hat{\Gamma}_m}{\hat{c}_n} - \hat{n}_e \frac{\hat{v}_i}{\hat{c}_n} \right) \frac{\sigma_{en}}{\sigma_0} \sqrt{\frac{8}{\pi} \hat{T}_e} \quad (8)$$

$$\hat{\omega}_c = \frac{qB}{m_e \nu_*} \quad ; \quad \hat{\nu}_e = \frac{\hat{\omega}_c^2}{\hat{\nu}_{en} + \alpha_B \hat{\omega}_c} \quad (9)$$

$$\nu_{ion} = \frac{n_n}{n_*} \sqrt{\frac{8}{\pi} \hat{T}_e} (1 + 2\hat{T}_e) \exp \left( -\frac{1}{\hat{T}_e} \right) \quad (10)$$

The non-dimensional ion velocity  $\hat{v}_i$ , electron density  $\hat{n}_e$ , electron temperature  $\hat{T}_e$ , and potential  $\hat{\phi}$  can be computed as:



$$\hat{T}_e = \frac{kT_e}{T_*} \quad ; \quad \hat{v}_i = \frac{v_i}{v_*} \quad ; \quad \hat{n}_e = \frac{n_e}{n_*} \quad ; \quad \hat{\phi} = \frac{e\phi}{T_*} \quad (11)$$

On the one hand, it can be observed that the ODEs given by Eq. (3), (4), and (5) have to be solved simultaneously, as each one depends on the others. On the other hand, the ODE for the non-dimensional potential can be solved independently once the other three parameters are determined. Nevertheless, in this project, we will solve all four simultaneously.

### 3.1 Question

**For the values of  $kT_{eB}/E_i = 0.08, 0.10, 0.12, 0.14, 0.16$ , plot the distributions of  $n_e$ ,  $\Gamma_i$ ,  $kT_e$ ,  $\phi$  and Mach number  $M$ .**

To address this question, a Matlab code has been implemented using the *ode45()* Matlab function to solve Eqs. (3), (4), (5), and (6). The integration with the *ode45()* Matlab function was performed until the Mach number reached 1, marking the sonic point previously mentioned and defining the end of the channel.

It is important to highlight that we encountered some issues with the initial value of  $kT_{eB}/E_i = 0.14$ . In this case, the first term of Eqs. (3), (4), (5), and (6) results in zero, leading to infinite values. To address this, a correction was applied to the initial value by adding  $10^{-7}$ , ensuring  $kT_{eB}/E_i = 0.14 + 10^{-7}$ .

Firstly, the code is employed to simultaneously solve  $\hat{v}_i$ ,  $\hat{n}_e$ ,  $\hat{T}_e$ , and  $\hat{\phi}$  along  $\hat{x}$  using the following initial values:

$$\hat{v}_i(0) = -\sqrt{\frac{5}{3} \frac{kT_{eB}}{E_i}} \quad ; \quad \hat{n}_e(0) = \frac{\Gamma_{iB}}{\Gamma_* \hat{v}_i(0)} \quad (12)$$

$$\hat{T}_e(0) = \frac{kT_{eB}}{E_i} \quad ; \quad \hat{\phi}(0) = 0 \quad (13)$$

Here,  $\Gamma_{iB} = -0.01\Gamma_m$ , with  $\Gamma_m = 6 \times 10^{22} \text{ m}^{-2} \text{ s}^{-1}$ . Once the non-dimensional values are solved until the Mach number reaches 1, the requested parameter in the exercise statement can be obtained as follows:

$$n_e = \hat{n}_e n_* \quad ; \quad \Gamma_i = \hat{v}_i \hat{n}_e \Gamma_* \quad ; \quad kT_e = \frac{\hat{T}_e T_*}{e} \text{ (eV)} \quad ; \quad \phi = \hat{\phi} \frac{T_*}{e} \quad (14)$$

$$M = \frac{\hat{v}_i}{\sqrt{\frac{5}{3} \hat{T}_e}} \quad ; \quad x = \hat{x} l_* \quad (15)$$

The results for electron density, ion flux density, electron energy, potential, and Mach number are presented in Fig. 4, 5, 6, 7, and 8. It is observed that the Mach number transitions from -1 to 1, as expected. Notably, the length of the channel where the sonic point is achieved varies for each initial value. A summary has been done in Table 1.

$kT_{eB}/E_i$	Sonic Point [mm]
0.08	14.60
0.10	7.62
0.12	5.10
$0.14 + 10^{-7}$	3.86
0.16	3.14

**Table 1:** For each initial value we address the sonic point in mm. The sonic point is considered when the Mach number reaches a value of 1.

The electron density increases across the channel until a certain point, indicating the start of propellant neutralization, which is expected at the end of the Hall Thruster to extract a positive net force for thrust production. The ion flux density exhibits a progressive increase, with an exponential rise at a certain point. This occurs when the potential undergoes a drastic decrease, accelerating ions and resulting in a faster ion velocity, giving a higher ion flux density. Lastly, the electron energy increases along the channel until a certain point, after which it starts to decrease. This change may be associated with the decrease in electron density, as energy depends on electron density.

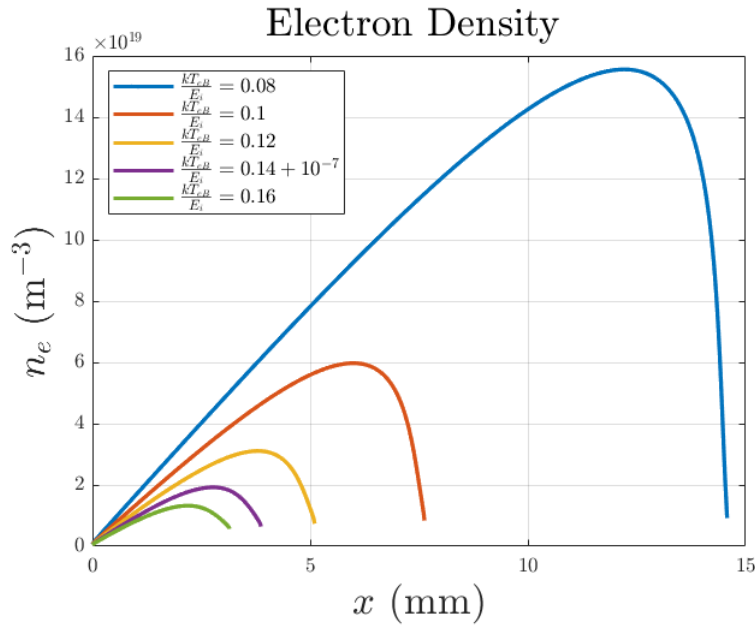


**Figure 4:** Electron density in  $\text{m}^{-3}$  vs channel length in mm for the five requested initial values.

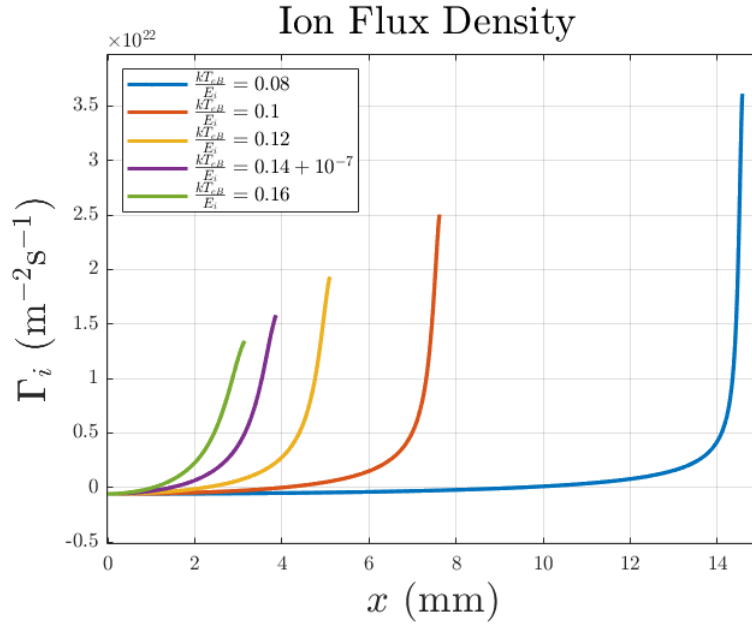


**Figure 5:** Ion flux density in  $\text{m}^{-2}\text{s}^{-1}$  vs channel length in mm for the five requested initial values.

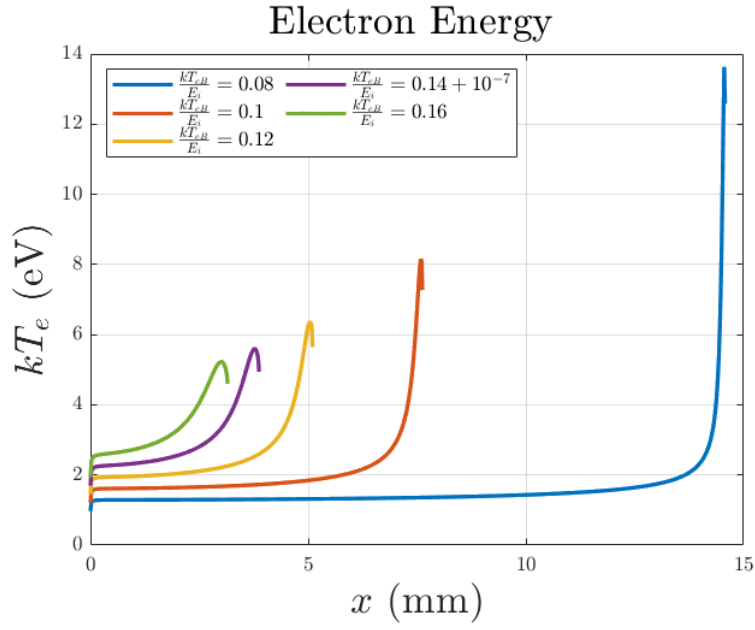


**Figure 6:** Electron energy in eV vs channel length in mm for the five requested initial values.

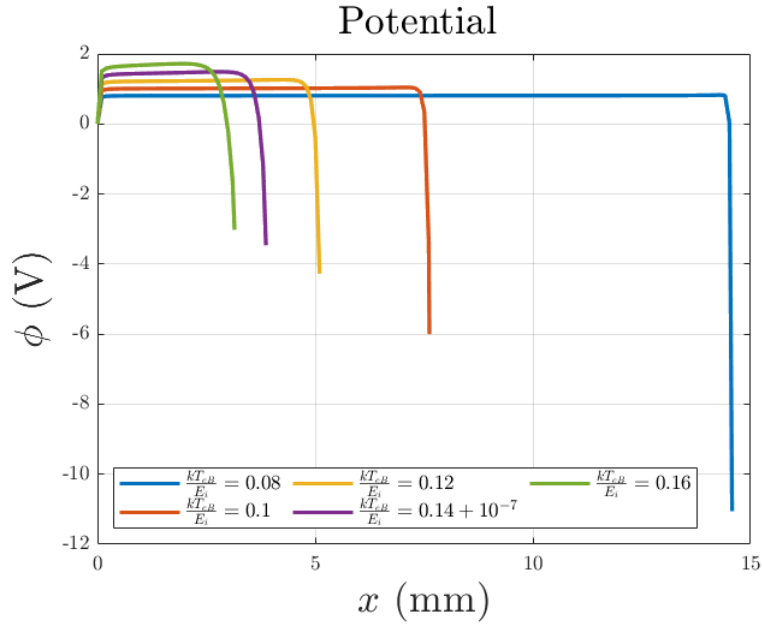


**Figure 7:** Potential in V vs channel length in mm for the five requested initial values.

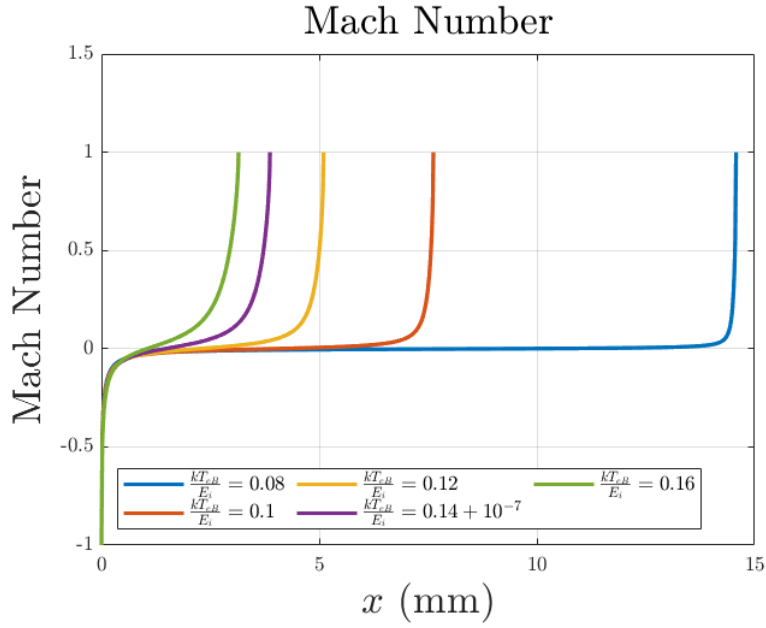


**Figure 8:** Mach number vs channel length in mm for the five requested initial values.

### 3.2 Question

Plot the utilization factor  $\eta_u$  and the back-streaming efficiency  $\eta_a$  Vs.  $\phi_E$ , with five points (each one corresponding to each value of  $kT_{eB}/E_i$  = of the previous question).

The utilization factor  $\eta_u$  is a factor that shows the ratio of ion mass flow to plasma mass flow, i.e. it penalises the neutral gas flow. It can be computed as:

$$\eta_u = \frac{\dot{m}_i}{\dot{m}} . \quad (16)$$

However, it is known that  $\dot{m} = \dot{m}_i + \dot{m}_n$ , so Eq. (16) can be expressed as:

$$\eta_u = \frac{(n_e/n_n)(c_i/c_n)}{1 + (n_e/n_n)(c_i/c_n)} , \quad (17)$$

where  $c_i$  and  $c_n$  are the escape velocities of ions and neutrals respectively and  $n_e$  and  $n_n$  are densities of electrons and neutrals.

In this case, the plasma is considered quasineutral, therefore  $n_n = n_i + n_e = 2n_e$ .

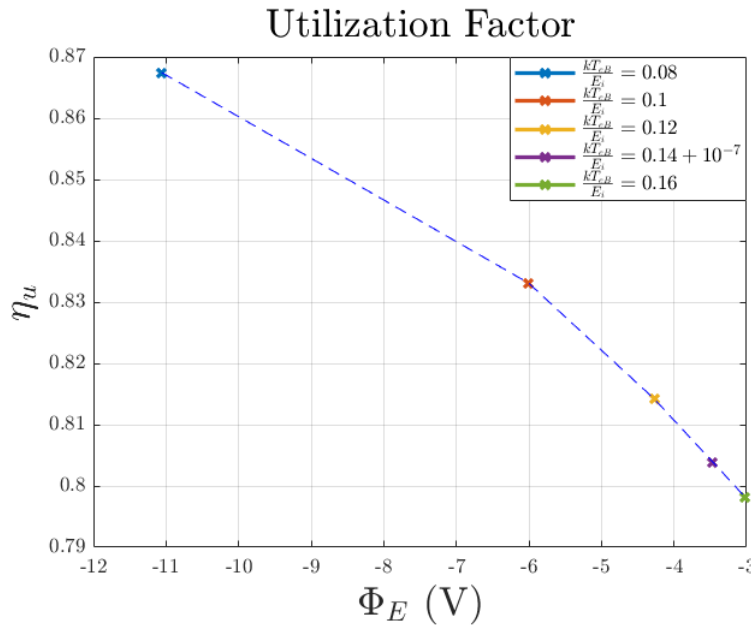


**Figure 9:** Utilization factor  $\eta_u$  as function of potential difference  $\Phi_E$ .

In Fig. 9 we can observe how for a lower initial condition we reach the highest mass flow ratio. This may be due to the fact that the potential difference is higher, so the ion velocity is also higher, which causes an increase in the utilization factor, as it depends on the exhaust velocity.

With regard to the back-streaming efficiency  $\eta_a$ , back-streaming efficiency in a Hall Thruster refers to the amount of ionised particles that escape from the system instead of

contributing to the desired thrust, so that the back-streaming of electrons is penalised and it is expected that the lower the electron leakage current, the higher the efficiency of our Hall Thruster. Therefore, to obtain this efficiency we use the following expressions:

$$\eta_a = 1 - \frac{I_{leak}}{I_a} . \quad (18)$$

$$\Gamma_d = \frac{n_e e (v_i - v_e) A}{A e} = \frac{I_a}{A e} , \quad (19)$$

where  $\Gamma_d$  is given by the statement of the problem (current density),  $A$  and  $e$  are constant values and  $I_a$  is the sum of beam current and the leakage (backstream) current.

The electron density in the region of acceleration is dependant on the flow of ions from the upstream ionization region, so the electron leakage current is:

$$I_{leak} = e n_e \frac{E}{B} \frac{\nu_e}{\omega_c} , \quad (20)$$

where  $\nu_e = 2/T_c = \omega_c/\pi$ . Then, by using Eqs. (18), (19) and (20) we obtain:

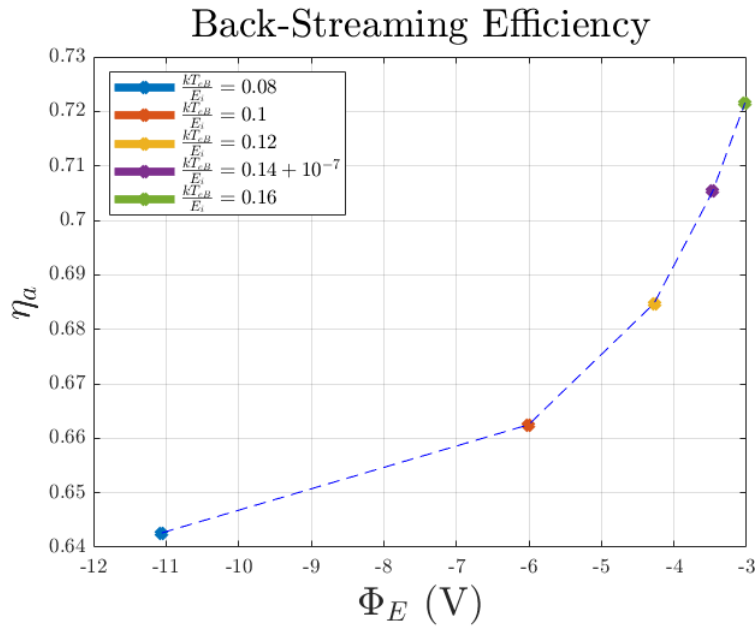


**Figure 10:** Back-Streaming efficiency  $\eta_a$  as function of potential difference  $\Phi_E$ .

As we can see in Fig. 10, back-streaming efficiency behaves in the opposite way to utilization factor, so that the higher the potential difference, the higher the leakage current

and therefore the lower the efficiency. This phenomena may be caused since as more potential difference, the higher is the velocity of the electrons, so they have more energy to escape from the discharge chamber and the plasma, not contributing to the thrust and increasing the leakage current.

### 3.3 Question

For the case  $kT_{eB}/E_i = 0.10$ , repeat the computations assuming the magnetic field depends on the axial coordinate according to

$$B(x) = 0.04 \exp \left[ - \left( \frac{x}{2l_*} - 0.5 \right)^2 \right] \quad (\text{T}) \quad (21)$$

Compute also the utilization factor  $\eta_u$  and the back-streaming efficiency  $\eta_a$ . Indicate the most noticeable differences with respect to the previous case for uniform magnetic field.

In this case, an axial magnetic field is imposed, as described in Eq. (21). The magnetic field follows a Gaussian form, as depicted in Fig. 11.

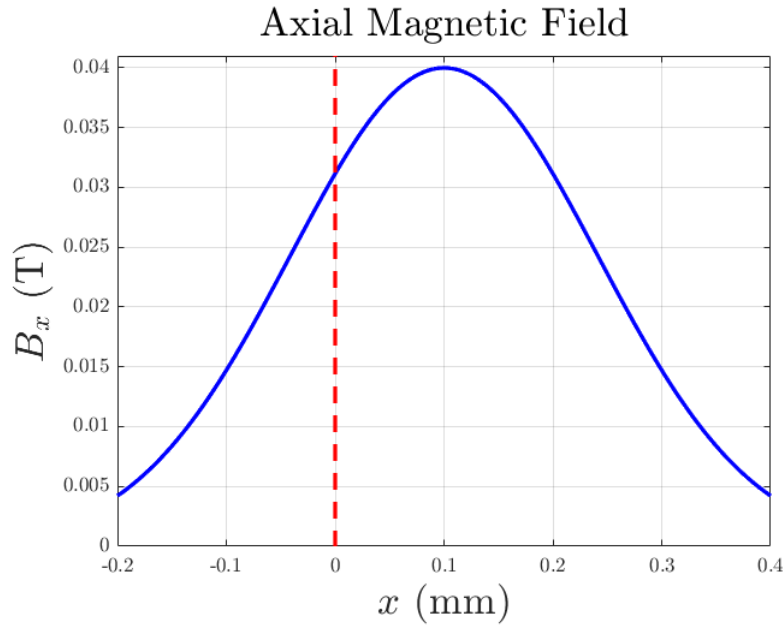
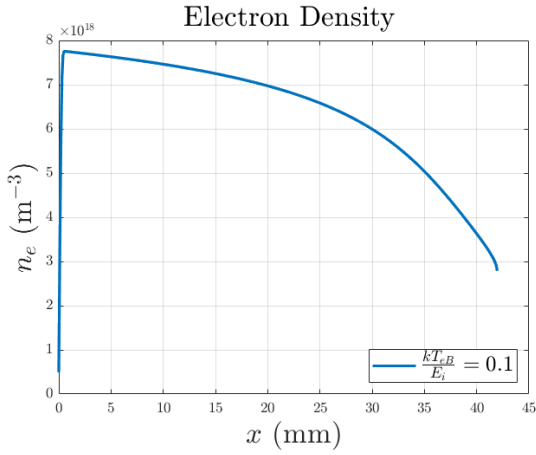


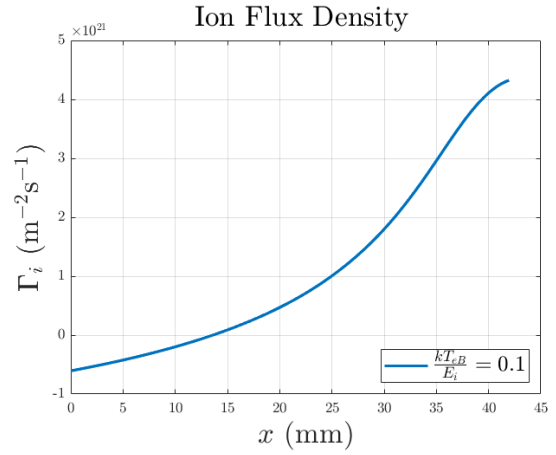
**Figure 11:** Axial magnetic field in Teslas vs channel lenght in millimetres. The red dashed line mars the  $x=0$  position, remarking the initial point on the Hall Thruster.

The magnetic field has a direct implication on the Larmor frequency, as evident in Eq. (9). The results for this case, with an initial value of  $kT_{eB}/E_i = 0.10$ , are depicted in Fig. 12a, 12b, 12c, 12d, and 13. The Mach number remains within the range of -1 to 1, and in this

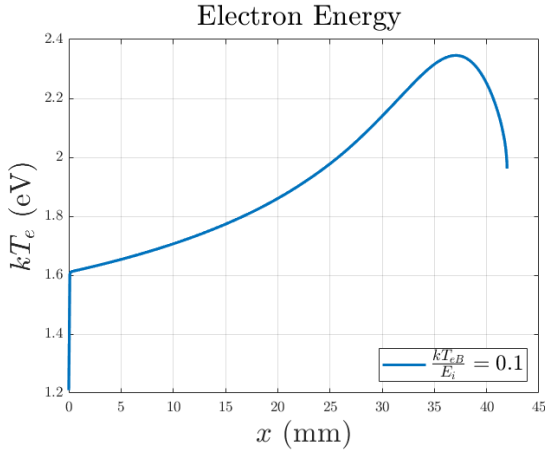
instance, the sonic point is located around 42 mm. The electron density increases rapidly due to the proximity to the maximum axial magnetic field, then drops as the magnetic field decreases to 0. The ion flux density increases along the channel, reaching higher values at the end of the channel. This is a consequence of the high voltage values obtained at the end of the channel. Finally, the electron energy increases across the channel until a certain point, after which it begins to decrease. This decrease may be attributed to the drop in electron density. We can generally observe than an initial peak appears in the result. This might be because of the maximum of the Gaussian axial magnetic field.



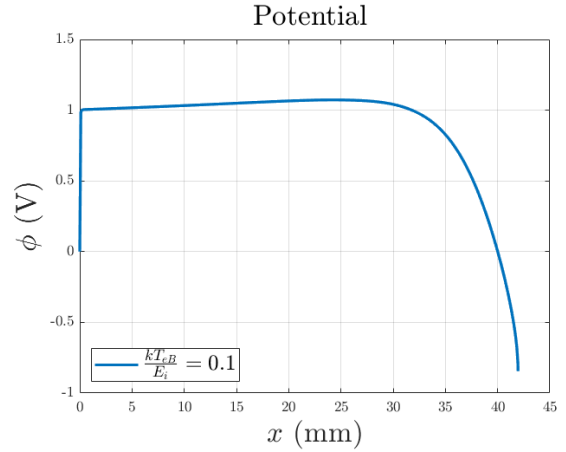
(a) Electron density in  $m^{-3}$  vs channel length in mm. In this case the used magnetic field is the one depicted in Fig. 11



(b) Ion flux density in  $m^{-2}s^{-1}$  vs channel length in mm. In this case the used magnetic field is the one depicted in Fig. 11.



(c) Electron energy in eV vs channel length in mm. In this case the used magnetic field is the one depicted in Fig. 11.



(d) Potential in V vs channel length in mm. In this case the used magnetic field is the one depicted in Fig. 11.



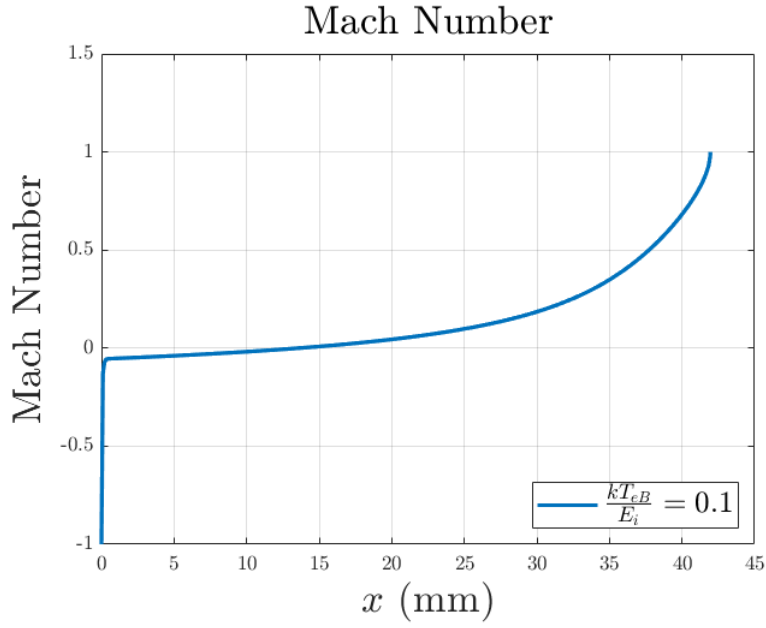


**Figure 13:** *Mach number vs channel length in mm. In this case the used magnetic field is the one depicted in Fig. 11.*

Regarding the utilization factor  $\eta_u$  and the back-streaming efficiency  $\eta_a$ , we obtain the following values:

$$\eta_u = 0.721 \quad , \quad \eta_a = 0.997 \quad .$$

We can appreciate how the utilization factor has decreased respect to the case with uniform magnetic field, whereas the back-streaming efficiency has increased to 99.7%. This may be due to the low potential difference between the anode and cathode, which means that the electrons do not have enough energy to escape from the discharge chamber and are therefore mostly used to ionise and ejected with the plasma, thus contributing to the thrust.

## 4 Conclusions

In this work we have performed a parametric analysis of the Hall Thruster using a one-dimensional model approximation. To do so, we have had to make a series of assumptions, as well as to use a series of equations that govern the behaviour of this type of thrusters in 1-D. In addition to this, an historical background was explained around the Hall Thruster, adding some state of the art Hall Thrusters as examples. Moreover, a brief description on how a Hall Thruster works was described.

The study begins with a non-dimensional analysis using fundamental magnitudes such as ionization energy, cross-sectional area, ion mass, and electron mass. Non-dimensional variables for velocity, rate of collisions, number density, and particle flux were defined to simplify the governing equations, such as velocity, electron density, electron temperature, and potential, which were expressed in a non-dimensional form. These ordinary differential equations (ODEs) were coupled and needed to be solved simultaneously.

To address the numerical analysis, a MATLAB code was implemented using the ode45 solver. The simulations were carried out for different initial values of  $kT_{eB}/E_i$ , specifically 0.08, 0.10, 0.12, 0.14, and 0.16.

The results demonstrated the evolution of electron density, ion flux density, electron energy, potential, and Mach number along the channel length. The Mach number transitioned from -1 to 1, marking the sonic point. Notably, the length of the channel where the sonic point was achieved varied for each initial value, as summarized in Table 1.

The utilization factor  $\eta_u$  and back-streaming efficiency  $\eta_a$  were computed for each simulation. The utilization factor showed a dependency on the potential difference  $\Phi_E$ , with higher initial conditions leading to increased mass flow ratios. Conversely, the back-streaming efficiency exhibited an inverse relationship with potential difference, suggesting that higher potential differences result in higher electron leakage current and lower efficiency.

The analysis was extended to include a non-uniform axial magnetic field described by a Gaussian distribution. The simulations were performed for the case with  $kT_{eB}/E_i = 0.10$ . The results indicated variations in electron density, ion flux density, electron energy, potential, and Mach number compared to the case with a uniform magnetic field.

For the case with a non-uniform magnetic field, the utilization factor decreased, and the back-streaming efficiency increased compared to the uniform field case. This suggests that the non-uniform magnetic field had an impact on the thruster performance, influencing the utilization of ions for thrust generation and the escape of electrons.

In summary, the numerical analysis provided insights into the behavior of a one-dimensional Hall Thruster under different conditions, highlighting the significance of magnetic field variations on the thruster's performance. The results contribute to a better understanding of the complex interplay between plasma and magnetic fields in Hall Thrusters, essential for optimizing their design and efficiency in practical applications.

## References

- [1] D. R. H. Goddard, *The Green Notebooks*, vol. 1. Clark University.
- [2] T. M. Mel’kumov, *Pioneers of Rocket Technology, Selected Works*. Academy of Sciences of the USSR, Institute for the History of Natural Science and Technology, 1964.
- [3] E. Stuhlinger, *Ion Propulsion for Space Flight*. 1964.
- [4] R. Jahn, *Physics of Electric Propulsion*. 1968.
- [5] A. Morozov, “The conceptual development of stationary plasma thrusters,” *Plasma Physics Reports*, vol. 29, pp. 235–250, 2003.
- [6] P. Y. Peterson, H. Kamhawi, W. Huang, G. Williams, J. H. Gilland, J. Yim, R. R. Hofer, and D. A. Herman, “Nasa’s hermes hall thruster electrical configuration characterization,” in *52nd AIAA/SAE/ASEE Joint Propulsion Conference*, p. 5027, 2016.
- [7] D. M. Goebel, I. Katz, and I. G. Mikellides, *Fundamentals of electric propulsion*. John Wiley & Sons, 2023.
- [8] J.-P. Boeuf, “Tutorial: Physics and modeling of hall thrusters,” *Journal of Applied Physics*, vol. 121, no. 1, 2017.
- [9] O. L. i Dalmases, “Module 6. lecture 1: Hall effect thrusters,” Course 2023-2024.